

specify the exact origin of this low-energy scattering process, although we speculate that it is caused by antiferromagnetic cobalt-rich oxide (Co<sub>3</sub>O<sub>4</sub>) on nanocrystal surfaces.

Because current through the nanocrystal array is carried by parallel conduction paths containing differing numbers of nanocrystals, the device magnetoresistance ratio is less sensitive to applied voltage. A plot of  $\Delta R/R_{\max}$  versus  $(V - V_T)$  (Fig. 4, inset) shows that for  $(V - V_T) = 900$  mV,  $\Delta R/R_{\max}$  is reduced to  $\sim 35\%$  of its maximum. Estimating  $n \sim 10$  nanocrystals in the shortest conduction path, this bias voltage implies an excess  $(V - V_T)n = 90$  mV across each junction. The corresponding effective temperature,  $e(90 \text{ meV})/k_B \sim 1000$  K, suppresses  $\Delta R/R_{\max}$  along this particular path. Parallel current paths through the array containing differing numbers of nanocrystals each have distinct voltage thresholds ( $V_{T\text{path}}$ ) for turn-on. Increasing bias voltage opens new current-carrying paths, so that whereas  $\Delta R/R_{\max}$  is suppressed for those channels where  $V > V_{T\text{path}}$ , the paths in which  $V$  is approximately equal to  $V_{T\text{path}}$  will continue to show strong magnetoresistance. This argument explains the experimental observation that bias voltage and temperature have a similar effect on  $\Delta R/R_{\max}$  in single magnetic-tunnel junctions (28), whereas measurements of granular magnetic thin films show  $\Delta R/R_{\max}$  is less sensitive to voltage (relative to temperature) (13).

Self-assembled Co-nanocrystal superlattices are model experimental systems for studying magnetotransport in nanostructured materials. The reported electrical measurements demonstrate spin-dependent tunneling in nanoscale devices formed of highly uniform magnetic-nanocrystal arrays.

References and Notes

1. J. C. Mallinson, *Magneto-Resistive Heads: Fundamentals and Applications* (Academic Press, New York, 1996), pp. 103–109.
2. S. S. P. Parkin et al., *J. Appl. Phys.* **85**, 5828 (1999).
3. J. S. Moodera, E. F. Gallagher, K. Robinson, J. Nowak, *Appl. Phys. Lett.* **70**, 3050 (1997).
4. S. Sun, C. B. Murray, D. Weller, L. Folks, A. Moser, *Science* **287**, 1989 (2000).
5. A. J. Rumberg, T. R. Ho, J. Clarke, *Phys. Rev. Lett.* **74**, 4714 (1995).
6. T. S. Tigue, M. T. Tuominen, J. M. Hergenrother, M. Tinkham, *Phys. Rev. B* **47**, 1145 (1993).
7. S. Sun, C. B. Murray, H. Doyle, *Mat. Res. Soc. Symp. Proc.* **577**, 395 (1999).
8. Similar devices containing nonmagnetic nanocrystals have been fabricated by R. P. Andres et al. [*Science* **273**, 1690 (1996)].
9. Local tunneling measurements of single Co-nanocrystals have been reported by C. Petit et al. [*Adv. Mater.* **11**, 1198 (1999)].
10. A. Bezryadin, R. M. Westervelt, M. Tinkham, *Appl. Phys. Lett.* **74**, 2699 (1999).
11. A. A. Middleton, N. S. Wingreen, *Phys. Rev. Lett.* **71**, 3198 (1993).
12. C. A. Neugebauer, M. B. Webb, *J. Appl. Phys.* **33**, 74 (1961).
13. D. L. Peng, K. Sumiyama, S. Yamamuro, T. Hihara, T. J. Konno, *Appl. Phys. Lett.* **74**, 76 (1999).
14. P. Sheng, B. Abeles, Y. Arie, *Phys. Rev. Lett.* **31**, 44 (1973).
15. B. Laikhtman, E. L. Wolf, *Phys. Lett. A* **139**, 257 (1989).

16. J. Robertson, in *Properties and Characterization of Carbon Films*, *Materials Science Forum*, **52–53**, J. J. Pouch, S. Alterovitz, Eds. (Trans Tech Publications, Brookfield, VT, 1990), pp. 125–151.
17. In 2D and 3D hexagonal arrays each nanocrystal has 6 and 12 nearest neighbors, respectively. In our devices the nanocrystal superlattice is one to three monolayers thick, so on average each nanocrystal has  $\sim 9$  nearest neighbors.
18. C. Lebreton et al., *Microelectron. Eng.* **41/42**, 507 (1998).
19. J. Inoue, S. Maekawa, *Phys. Rev. B* **53**, 11927 (1996).
20. R. Meservey, P. M. Tedrow, *Phys. Rev. B* **7**, 318 (1973).
21. T. Zhu, Y. J. Wang, *Phys. Rev. B* **60**, 11918 (1999).
22. S. Mitani et al., *Phys. Rev. Lett.* **81**, 2799 (1998).

23. S. Mitani, H. Fujimori, S. Ohnuma, *J. Magn. Magn. Mater.* **177–181**, 919 (1998).
24. H. Bruckl et al., *Phys. Rev. B* **58**, 8893 (1998).
25. S. Takahashi, S. Maekawa, *J. Magn. Magn. Mater.* **198–199**, 143 (1999).
26. J. M. D. Coey, A. E. Berkowitz, L. I. Balcells, F. F. Putris, A. Barry, *Phys. Rev. Lett.* **80**, 3815 (1998).
27. R. Jansen, J. S. Moodera, *J. Appl. Phys.* **83**, 6682 (1998).
28. N. Tezuka, T. Miyazaki, *Jpn. J. Appl. Phys.* **37**, L218 (1998).
29. We thank C. Kagan for helpful discussions and for critical readings of this manuscript.

10 July 2000; accepted 29 September 2000

# The Role of Mg<sup>2+</sup> as an Impurity in Calcite Growth

Kevin J. Davis,<sup>1</sup> Patricia M. Dove,<sup>1\*</sup> James J. De Yoreo<sup>2</sup>

Magnesium is a key determinant in CaCO<sub>3</sub> mineralization; however, macroscopic observations have failed to provide a clear physical understanding of how magnesium modifies carbonate growth. Atomic force microscopy was used to resolve the mechanism of calcite inhibition by magnesium through molecular-scale determination of the thermodynamic and kinetic controls of magnesium on calcite formation. Comparison of directly measured step velocities to standard impurity models demonstrated that enhanced mineral solubility through magnesium incorporation inhibited calcite growth. Terrace width measurements on calcite growth spirals were consistent with a decrease in effective supersaturation due to magnesium incorporation. Ca<sub>1-x</sub>Mg<sub>x</sub>CO<sub>3</sub> solubilities determined from microscopic observations of step dynamics can thus be linked to macroscopic measurements.

Magnesium is an important modifier of CaCO<sub>3</sub> morphology and growth in natural waters (1–3). Accordingly, changes in the seawater Mg/Ca ratio may have governed the polymorphic transitions observed in carbonate biominerals during the geologic past (4, 5). Although the presence of Mg<sup>2+</sup> in calcium carbonate biominerals is increasingly being used as an empirical paleothermometer (6–10), the physical basis by which Mg<sup>2+</sup> modifies carbonate growth has yet to be discerned. Bulk studies have suggested that calcite growth is inhibited through either step-blocking by Mg<sup>2+</sup> adsorption and slow dehydration (11–14) or enhanced mineral solubility associated with Mg<sup>2+</sup> incorporation (15). Here we address this controversy over the molecular-scale mechanism by which Mg<sup>2+</sup> inhibits calcite growth, by comparing in situ experimental measurements to theoretical crystal growth impurity models.

We used fluid-cell atomic force microscopy (AFM) to make in situ observations of

calcite crystallization onto a seed crystal in a flow-through environment (16). Single-sourced growth spirals emanating from screw dislocations on the calcite surface were imaged in Contact Mode (Digital Instruments, Santa Barbara) under controlled solution conditions at 25°C. Supersaturated growth solutions were prepared from CaCl<sub>2</sub> and NaHCO<sub>3</sub>. Mg<sup>2+</sup> was introduced to the growth solutions as MgCl<sub>2</sub>, and inductively coupled plasma-atomic emission spectroscopy was used to confirm the purity of all reactants. The pH of each growth solution was adjusted to 8.50 by small additions of NaOH (17). The ionic strength of each solution was fixed between 0.115 and 0.119 M, and the ratio of calcium-to-carbonate activity was held from 0.99 to 1.01. The chemical speciation of each solution was modeled by means of a numerical code that implemented the Davies equation for activity determinations (18). Monomolecular step velocities ( $v_s$ ) and terrace widths ( $\lambda$ ) were directly measured on growth spirals as a function of both supersaturation ( $\sigma$ ) and Mg<sup>2+</sup> activity. The rate of solution input was adjusted to yield step velocities that were independent of flow rate, thereby ensuring that growth was not limited by mass transport to the surface. Step velocity was determined as displacement from a fixed reference point (i.e., the dislocation source)

<sup>1</sup>Department of Geological Sciences, Virginia Polytechnic Institute and State University, Blacksburg, VA 24061, USA. <sup>2</sup>Department of Chemistry and Materials Science, Lawrence Livermore National Laboratory, Livermore, CA 94550, USA.

\*To whom correspondence should be addressed. E-mail: dove@vt.edu

## REPORTS

or by changes in the apparent step orientation (19). Terrace widths were determined by measuring the distance between adjacent steps on the growth spiral.

The supersaturation,  $\sigma$ , is defined by

$$\sigma \equiv \frac{\Delta\mu}{k_B T} = \ln\left(\frac{a}{a_e}\right) \quad (1a)$$

or for  $\text{CaCO}_3$  in aqueous solution

$$\sigma = \ln\left(\frac{a_{\text{Ca}^{2+}} a_{\text{CO}_3^{2-}}}{K_{\text{sp}}}\right) \quad (1b)$$

where  $\Delta\mu$  is the change in chemical potential per molecule,  $k_B$  is the Boltzmann constant,  $T$  is absolute temperature,  $a$  and  $a_e$  are actual and equilibrium activity products,  $a_{\text{Ca}^{2+}}$  is the activity of  $\text{Ca}^{2+}$ ,  $a_{\text{CO}_3^{2-}}$  is the activity of  $\text{CO}_3^{2-}$ , and  $K_{\text{sp}}$  is the equilibrium solubility product at the ionic strength of the experimental solutions.  $K_{\text{sp}}$  ( $10^{-8.48}$ ) was calculated from the activities at which measured step speeds went to zero. The supersaturations in this study were reported relative to the solubility of pure calcite, with the use of this  $K_{\text{sp}}$  value. We made in situ measurements for a suite of unique solution compositions where  $\sigma = 0.98, 1.20,$  and  $1.40$  at various  $\text{Mg}^{2+}$  impurity concentrations.

Layer growth of calcite was observed as the migration of atomically flat steps generated at dislocations on the  $\{10\bar{1}4\}$  cleavage surface. The advancement of these  $3.1 \text{ \AA}$  monomolecular steps resulted in the formation of polygonal growth hillocks with steps parallel to the  $\langle\bar{4}41\rangle$  directions (Fig. 1A). The  $c$ -glide symmetry plane generated two distinct pairs of crystallographically identical steps denoted as the positive ( $[\bar{4}41]_+$  and  $[48\bar{1}]_+$ ) and negative directions ( $[\bar{4}41]_-$  and  $[48\bar{1}]_-$ ) (20). These two step types have different step-edge geometries and kink site structures because of differences in the orientation of the exposed carbonate groups (20).

Calcite spirals grown in the absence of  $\text{Mg}^{2+}$  were characterized by well-formed vicinal faces with straight step-edges (Fig. 1, A and B). The addition of  $\text{Mg}^{2+}$  to the growth solutions caused step-edges to roughen and prefer-

entially affected those steps along the negative direction (Fig. 1C). Although these results (Fig. 1C) indicate that  $\text{Mg}^{2+}$  modifies the kink-site activity at step-edges, the mechanism of this interaction cannot be discerned from images of hillock morphology alone. The underlying physical basis for these morphological observations may be determined by measuring the thermodynamic and kinetic manifestations of crystallization, terrace width ( $\lambda$ ), and step velocity ( $v_s$ ), respectively.

Examination of step velocity data in the context of crystal growth impurity models allows for rigorous determination of the molecular-scale mechanism for calcite inhibition by  $\text{Mg}^{2+}$ . The two dominant impurity models, and those most appropriate for explaining the conflicting macroscopic observations of the  $\text{Ca}_{1-x}\text{Mg}_x\text{CO}_3$  system, are presented in Fig. 2. Step pinning or blocking occurs when impurity molecules adsorb to step-edges or accumulate on terraces ahead of migrating steps, thereby decreasing the velocity of those steps (Fig. 2A). Based on the classic theory of Cabrera and Vermilyea (21), this model predicts a dead zone of supersaturation where the steps fail to advance and no growth is observed. When a threshold supersaturation is met, the steps break through the chain of adsorbed impurities and rapidly achieve the step velocity ( $v_s$ ) characteristic of the pure system. Greater impurity concentrations ( $C_i$ ) result in a wider dead zone.

In contrast, impurity incorporation occurs when foreign ions or molecules become captured by advancing steps or otherwise incorporate at kink sites along a step-edge to become part of the growing crystal. The incorporation of impurity molecules induces strain in the solid lattice, thereby increasing the internal free energy of the crystal (22, 23). The resultant increase in crystal solubility reduces the reaction affinity by decreasing the effective supersaturation ( $\sigma_{\text{eff}}$ ) of the growth solution. This shifts the apparent thermodynamic equilibrium of the system toward higher growth-unit activities so that steps never achieve velocities characteristic of the pure system (Fig. 2B). Higher impurity con-

centrations lead to increased incorporation and corresponding shifts in the thermodynamic equilibrium of the system. This behavior is observed for our measured dependence of  $v_s$  on supersaturation for the various  $\text{Mg}^{2+}$  levels (Fig. 3). For each  $\text{Mg}^{2+}$  concentration, the dependence of  $v_s$  upon  $a_{\text{Ca}^{2+}}$  is similar to that of the pure system but shifted toward higher equilibrium activities. The linear portion of these curves is predicted by classic crystal growth theory according to

$$v_s = \beta\omega(a - a_e) \quad (2)$$

where  $\beta$  is the kinetic coefficient,  $\omega$  is the specific molecular volume of calcite ( $6.13 \times 10^{-23} \text{ cm}^3$  per molecule), and  $(a - a_e)$  is the difference in growth-unit activity from equilibrium (24, 25). Direct measurements of the equilibrium activity ( $a_e$ ) at which steps were observed neither to advance nor retreat in the pure system revealed curvature in the  $v_s$  versus  $(a - a_e)$  dependence at low  $a_{\text{Ca}^{2+}}$  (dashed lines). This curvature is expected to be caused by the presence of background impurities in the growth solutions (26) or nonlinear attachment/detachment kinetics at low supersaturation (27). Because near-equilibrium measurements of step speed in the presence of  $\text{Mg}^{2+}$  demonstrated the same curvature as that found for the pure system (see data for  $64\times\text{Mg}$  in Fig. 3), subsequent equilibrium activities ( $a_e$ ) for each  $\text{Mg}^{2+}$  concentration were extrapolated from the kinetic data by means of this curvature.

Comparison of the experimental kinetic plot (Fig. 3) to the theoretical impurity models (Fig. 2, A and B) indicates that  $\text{Mg}^{2+}$  inhibits calcite growth through an incorporation mechanism. As the  $\text{Mg}^{2+}$  concentration increases in the growth solutions, larger amounts of  $\text{Mg}^{2+}$  enter the calcite lattice, enhancing the solubility of the growing crystal. This causes the growth solutions to exhibit a lower effective supersaturation ( $\sigma_{\text{eff}}$ ) as the equilibrium point of the system is shifted toward higher activities. The shift in equilibrium activity accounts for the region of apparent positive supersaturation where no growth occurs and the slower growth rate

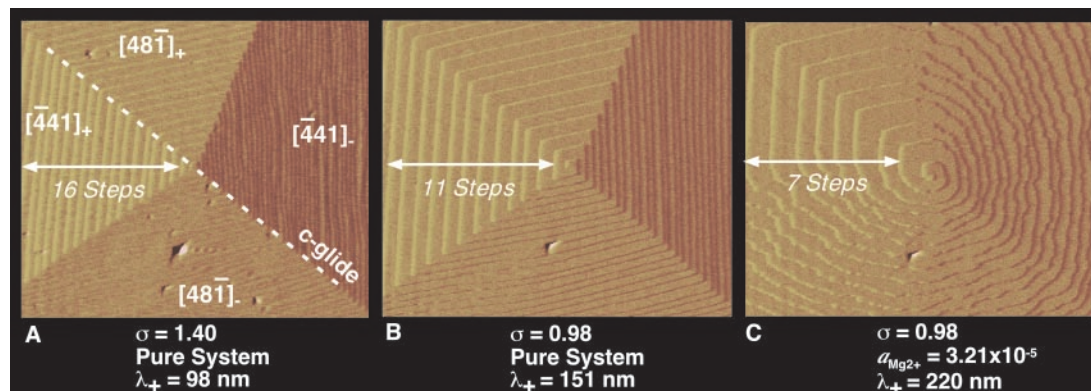


**Fig. 1.** (A to C) AFM images of a calcite growth hillock illustrating the effect of supersaturation ( $\sigma$ ) and  $\text{Mg}^{2+}$  on terrace width ( $\lambda$ ). Decreasing  $\sigma$  or increasing  $a_{\text{Mg}^{2+}}$  results in wider step terraces, shown here as a decrease in step density. All images are  $3 \mu\text{m}$  by  $3.5 \mu\text{m}$ ; step height is  $3.1 \text{ \AA}$ .

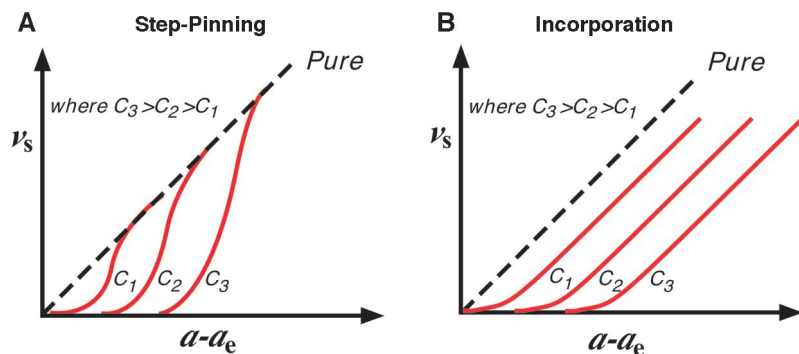


**Fig. 2.** (A and B) Theoretical crystal growth impurity models illustrating the dependence of step velocity ( $v_s$ ) on supersaturation ( $a - a_e$ ), where  $C_i$  is the aqueous impurity concentration. Here, supersaturation is expressed as the difference in growth-unit activity ( $a$ ) from its equilibrium value ( $a_e$ ).

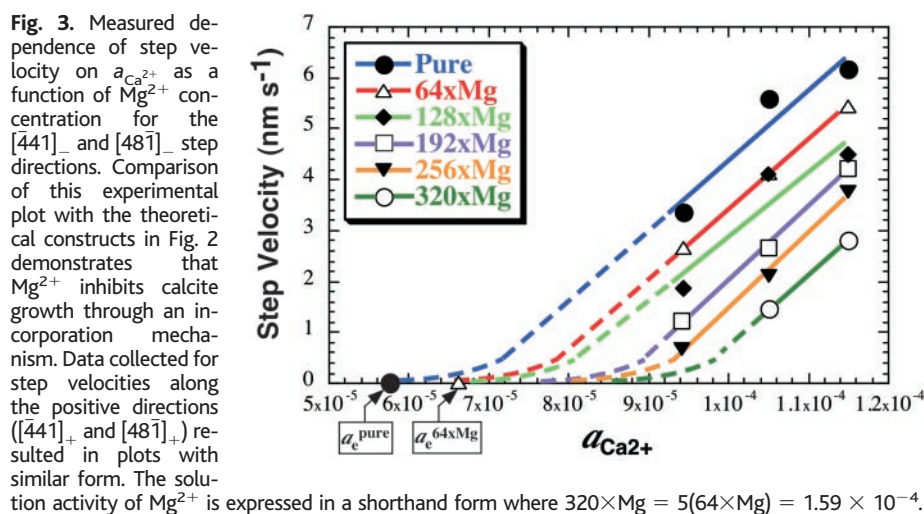


**Fig. 3.** Measured dependence of step velocity on  $a_{\text{Ca}^{2+}}$  as a function of  $\text{Mg}^{2+}$  concentration for the  $[441]_-$  and  $[481]_-$  step directions. Comparison of this experimental plot with the theoretical constructs in Fig. 2 demonstrates that  $\text{Mg}^{2+}$  inhibits calcite growth through an incorporation mechanism. Data collected for step velocities along the positive directions ( $[441]_+$  and  $[481]_+$ ) resulted in plots with similar form. The solution activity of  $\text{Mg}^{2+}$  is expressed in a shorthand form where  $320 \times \text{Mg} = 5(64 \times \text{Mg}) = 1.59 \times 10^{-4}$ .

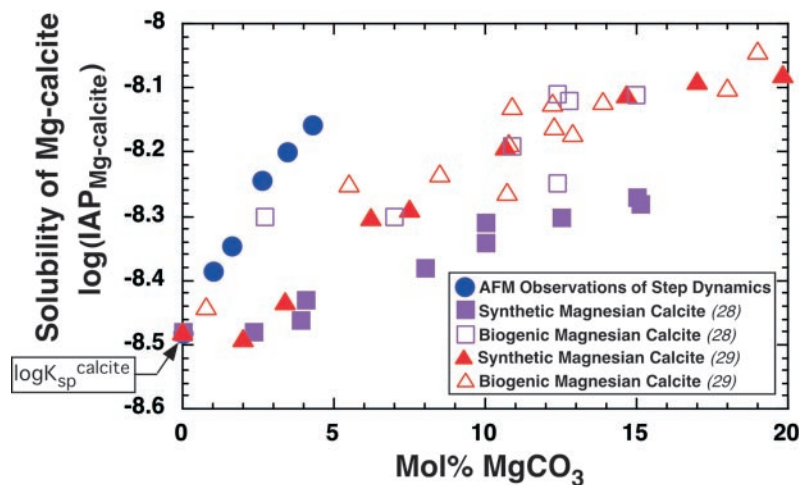


**Fig. 4.** Comparison of  $\text{Ca}_{1-x}\text{Mg}_x\text{CO}_3$  solubilities determined from microscopic observations of monomolecular step dynamics (this study) to those measured by macroscopic methods (28, 29). Solubilities are expressed as  $\text{IAP}_{\text{Mg-calcite}} = (a_{\text{Ca}^{2+}})(a_{\text{CO}_3^{2-}})$ .

observed in the presence of  $\text{Mg}^{2+}$ . The slope of the step velocity versus  $a_{\text{Ca}^{2+}}$  curves does not vary, indicating that the molecular attachment/detachment kinetics (as expressed through  $\beta$  in Eq. 2) are unchanged by  $\text{Mg}^{2+}$ .

Terrace width ( $\lambda$ ) measurements made in

parallel with these kinetic observations provided an independent test of whether  $\text{Mg}^{2+}$  shifts the thermodynamic properties of the system. Decreasing the supersaturation of the growth solutions increased terrace widths, resulting in a decrease in the density of steps on

the spiral hillock (Fig. 1, A and B). Increasing solution concentrations of  $\text{Mg}^{2+}$  at constant  $\sigma$  likewise caused terrace widths to increase (Fig. 1, B and C). Thus, the addition of  $\text{Mg}^{2+}$  to the growth solutions was found to have a similar effect on measured terrace widths, as did a simple reduction in supersaturation. These thermodynamic observations are predicted by the following expression of the Gibbs-Thomson relation:

$$\lambda = \frac{2.04\Gamma\omega\alpha}{k_B T \sigma} \quad (3)$$

where  $\lambda$  is the terrace width (nm),  $\Gamma$  is a factor that takes into account the dependence of step speed on step length,  $\omega$  is the specific molecular volume,  $\alpha$  is the step-edge free energy per unit step height [appropriately averaged over a full turn of the growth spiral (16)],  $k_B$  is the Boltzmann constant,  $T$  is the temperature (K),  $\sigma$  is the previously defined supersaturation, and the quantity 2.04 is a factor related to the geometry of the calcite hillock (16). According to this expression, the observed increase in terrace width with the addition of  $\text{Mg}^{2+}$  is consistent with a decrease in the effective supersaturation ( $\sigma_{\text{eff}}$ ) of the growth solutions due to enhanced mineral solubility.

Our step velocity and terrace width measurements independently demonstrate that  $\text{Mg}^{2+}$  inhibits calcite growth by incorporating into the  $\text{CaCO}_3$  lattice. The resultant increase in mineral solubility forms the underlying physical basis for the reduced calcite growth rates observed in the presence of  $\text{Mg}^{2+}$ . Accordingly, a thorough understanding of the Ca-Mg- $\text{CO}_2$  system requires an accurate assessment of the extent to which  $\text{Mg}^{2+}$  modifies calcite solubility. The equilibrium activities ( $a_e$ ) determined in this study as a function of  $\text{Mg}^{2+}$  concentration represent molecular-scale measurements of magnesian calcite solubilities. These microscopic solubility determinations were correlated with electron microprobe measurements of the  $\text{Mg}^{2+}$  content of the crystals and compared to solubilities determined by macroscopic methods (Fig. 4). While all investigators (28, 29), including the present study, measured an equivalent solubility for pure calcite ( $10^{-8.48}$ ), the  $\text{Ca}_{1-x}\text{Mg}_x\text{CO}_3$  solubilities determined from direct observations of step dynamics were higher than solubilities from macroscopic experiments. The discrepancy may be attributed to the vast experimental differences between monitoring the migration of monomolecular steps and macroscopic methods (30). Only by linking these macroscopic thermodynamic properties to direct observations of step dynamics at the nanometric scale can we conclude that  $\text{Mg}^{2+}$  inhibits calcite growth by altering the equilibrium thermodynamics of the new growth surface through incorporation. Resolving the molecular-scale mechanism by which  $\text{Mg}^{2+}$  inhibits

calcite growth is an important first step toward establishing a physical model for the thermodynamic and kinetic consequences of Mg<sup>2+</sup> incorporation during biomineral formation.

References and Notes

1. K. De Groot, E. M. Duyvis, *Nature* **212**, 183 (1966).
2. R. L. Folk, *J. Sediment. Petrol.* **44**, 40 (1974).
3. R. W. Lahann, *J. Sediment. Petrol.* **48**, 337 (1978).
4. S. M. Stanley, L. A. Hardie, *Palaeogeogr. Palaeoclimatol. Palaeoecol.* **144**, 3 (1998).
5. S. M. Stanley, L. A. Hardie, *GSA Today* **9**, 1 (1999).
6. G. S. Dwyer et al., *Science* **270**, 1347 (1995).
7. T. Mitsuguchi, E. Matsumoto, O. Abe, T. Uchida, P. J. Isdale, *Science* **274**, 961 (1996).
8. L. M. A. Purton, G. A. Shields, M. D. Brasier, G. W. Grime, *Geology* **27**, 1083 (1999).
9. C. H. Lear, H. Elderfield, P. A. Wilson, *Science* **287**, 269 (2000).
10. H. Elderfield, G. Ganssen, *Nature* **405**, 442 (2000).
11. M. M. Reddy, K. K. Wang, *J. Cryst. Growth* **50**, 470 (1980).
12. A. Mucci, J. W. Morse, *Geochim. Cosmochim. Acta* **47**, 217 (1983).
13. M. M. Reddy, in *U.S. Geol. Surv. Bull. 1578: Studies in Diagenesis*, F. A. Mumpton, Ed. (1986), pp. 169–182.

14. A. Gutjahr, H. Dabringhaus, R. Lacmann, *J. Cryst. Growth* **158**, 310 (1996).
15. R. A. Berner, *Geochim. Cosmochim. Acta* **39**, 489 (1975).
16. H. H. Teng, P. M. Dove, C. A. Orme, J. J. De Yoreo, *Science* **282**, 724 (1998).
17. The solution pH did not drift perceptibly during precipitation due to the extremely short residence times (6 s) used in this flow-through experimental configuration.
18. C. Papelis, K. F. Hayes, J. O. Leckie, *Tech. Rep. 306* (Department of Civil Engineering, Stanford University, 1988).
19. T. A. Land, J. J. De Yoreo, J. D. Lee, *Surf. Sci.* **384**, 136 (1997).
20. J. Paquette, R. J. Reeder, *Geochim. Cosmochim. Acta* **59**, 735 (1995).
21. N. Cabrera, D. A. Vermilyea, in *Growth and Perfection of Crystals* (Chapman & Hall, London, 1958), p. 393.
22. V. V. Voronkov, L. N. Rashkovich, *Sov. Phys. Crystallogr.* **37**, 289 (1992).
23. W. J. P. van Enckevort, A. C. J. F. van den Berg, *J. Cryst. Growth* **183**, 441 (1998).
24. W. K. Burton, N. Cabrera, F. C. Frank, *Philos. Trans. R. Soc. London* **243**, 299 (1951).
25. A. A. Chernov, *Soviet Phys.* **4**, 116 (1961).
26. H. H. Teng, P. M. Dove, J. J. De Yoreo, *Geochim. Cosmochim. Acta* **63**, 2507 (1999).

27. J. J. De Yoreo, C. A. Orme, G. S. Bales, unpublished results.
28. W. D. Bischoff, F. T. Mackenzie, F. C. Bishop, *Geochim. Cosmochim. Acta* **51**, 1413 (1987).
29. E. Busenberg, L. N. Plummer, *Geochim. Cosmochim. Acta* **53**, 1189 (1989).
30. We examined layer growth on the {10 $\bar{1}$ 4} face of calcite, while macroscopic measurements of solubility were determined from a composite of different surfaces. Nonequilibrium facets are generated by collisional fracture in mass crystallizers or are caused by the presence of Mg<sup>2+</sup> and other impurities in the growth solution (2, 3, 37). Because the present study pertains to only one crystallographic facet, a direct solubility comparison is not valid.
31. J. O. Titiloye, S. C. Parker, D. J. Osguthorpe, S. Mann, *J. Chem. Soc. Chem. Commun.* 1494 (1991).
32. This work was performed under the auspices of the U.S. Department of Energy, Division of Geosciences and Engineering, by the Georgia Institute of Technology (DE-FG02-98ER14843) and Lawrence Livermore National Laboratory under contract W-7405-Eng-48. K.J.D. thanks the Mayo Educational Foundation of the Southeast Federation of Mineralogical Societies for personal support during this project.

20 July 2000; accepted 29 September 2000

# African Hot Spot Volcanism: Small-Scale Convection in the Upper Mantle Beneath Cratons

Scott D. King<sup>1\*</sup> and Jeroen Ritsema<sup>2</sup>

Numerical models demonstrate that small-scale convection develops in the upper mantle beneath the transition of thick cratonic lithosphere and thin oceanic lithosphere. These models explain the location and geochemical characteristics of intraplate volcanos on the African and South American plates. They also explain the presence of relatively high seismic shear wave velocities (cold downwellings) in the mantle transition zone beneath the western margin of African cratons and the eastern margin of South American cratons. Small-scale, edge-driven convection is an alternative to plumes for explaining intraplate African and South American hot spot volcanism, and small-scale convection is consistent with mantle downwellings beneath the African and South American lithosphere.

Cratons are regions of continents that have not been affected by tectonic processes for more than one billion years. Relatively low surface heat flow (1), diamond inclusions in kimberlites (2), and a relatively cold and thick keel (3) with high seismic velocities to about 250 km depth (4) distinguish cratons from other continental lithosphere. Although cratons are commonly envisioned as stable regions of Earth's lithosphere, the change in lithospheric thickness and, hence, the relatively strong lateral temperature and viscosity contrasts at the edges of cratons induce a

small-scale form of convective flow in the mantle beneath the craton margin. Numerical (5) and laboratory (6) investigations indicate that such convective flow, commonly termed edge-driven convection, consists of down-

wellings extending as deep as the mantle transition zone (about 660 km) beneath the margins of cratons and upwellings at about 500 to 1000 km distance from the margins of cratons. Previous workers have suggested that edge-driven convection may be responsible for the formation of the Bermuda Rise (7), the North Atlantic Tertiary Volcanics (8), and flood basalt magmatism at the peripheries of cratonic provinces (9). Here, we suggest that intraplate volcanos (hot spots) on the African and South American plates (Fig. 1) are linked to edge-driven convection on the basis of numerical simulations of mantle flow and images of seismic velocity anomalies in the African upper mantle.

Our model of edge-driven convection is based on the temperature and velocity fields, computed using a compressible convection formulation for a two-dimensional Cartesian geometry (Fig. 2) (10). The initial thermal structure of an ocean basin is calculated using the solution for a moving plate, whereas the thermal structure of the cratonic lithosphere is calculated using the half-space solution and assuming that the

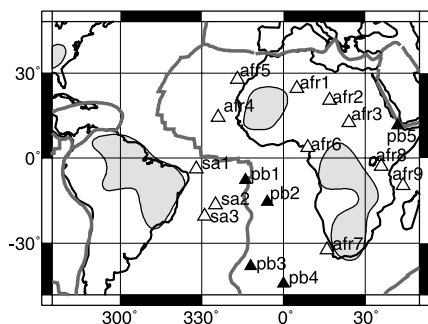


**Fig. 1.** Location of hot spots (triangles), cratons (gray shading), and plate boundaries (gray line). The boundaries of cratons are defined seismically: they circumscribe regions of S20RTS at 100 km depth where the shear wave velocity perturbation from the PREM model is 4% or larger. The hotspots are taken from the list compiled by Sleep (20). The intraplate "African hot spots" are denoted by white triangles (afr1, Ahaggar; afr2, Tibesti; afr3, Jebel Mara; afr4, Cape Verde; afr5, Canary; afr6, Mt Cameroon; afr7, Vema; afr8, Victoria; and afr9, Comores), as are the "South American" hotspots (sa1, Fernando; sa2, Arnold; and sa3, Trinidad). "Plate Boundary" hot spots are denoted with black triangles (pb1, Ascension; pb2, St. Helena; pb3, Tristan da Cunha; pb4, Discovery; and pb5, Afar).

<sup>1</sup>Department of Earth and Atmospheric Sciences, Purdue University, West Lafayette, IN 47907-1397, USA.  
<sup>2</sup>Seismological Laboratory, California Institute of Technology, Pasadena, CA 91125, USA.

\*To whom correspondence should be addressed. E-mail: sking@purdue.edu